

600 km repeater-like quantum communications with dual-band stabilisation

Mirko Pittaluga^{1,2†*}, Mariella Minder^{1,3†}, Marco Lucamarini^{1,4*}, Mirko Sanzaro¹,
Robert I. Woodward¹, Ming-Jun Li⁵, Zhiliang Yuan¹ & Andrew J. Shields¹

¹*Toshiba Europe Limited, 208 Cambridge Science Park,
Cambridge CB4 0GZ, UK*

²*School of Electronic and Electrical Engineering,
University of Leeds, Leeds LS2 9JT, UK*

³*Department of Engineering, Cambridge University,
9JJ Thomson Avenue, Cambridge CB3 0FA, UK*

⁴*Department of Physics and York Centre for Quantum Technologies,
University of York, York YO10 5DD, UK*

⁵*Corning Incorporated, Corning, New York, 14831, USA*

[†]*These authors contributed equally to this work*

**mirko.pittaluga@crl.toshiba.co.uk*

**marco.lucamarini@york.ac.uk*

Twin-field (TF) quantum key distribution (QKD) fundamentally alters the rate-distance relationship of QKD, offering the scaling of a single-node quantum repeater. Although recent experiments have demonstrated the new opportunities for secure long-distance communications allowed by TF-QKD, formidable challenges remain to unlock its true potential. Previous demonstrations have required intense stabilisation signals at the same wavelength as the quantum signals, thereby unavoidably generating Rayleigh scattering noise that limits the distance and bit rate. Here, we introduce a novel dual-band stabilisation scheme that overcomes past limitations and can be adapted to other phase-sensitive single-photon applications. Using two different optical wavelengths multiplexed together for channel stabilisation and protocol encoding, we develop a setup that provides repeater-like key rates over record communication distances of 555 km and 605 km in the finite-size and asymptotic regimes respectively, and increases the secure key rate at long distance by two orders of magnitude to values of practical significance.

INTRODUCTION

Quantum key distribution (QKD) [1, 2] allows two distant users to establish a common secret string of bits by sending photons through a communication line, often an optical fibre. The photons, however, are scattered by the propagation medium and have only a small probability of reaching the end of the line, which restrains the QKD key rate and transmission range. A rigorous theorem [3] (see also [4]) limits to 1.44η the number of secure bits delivered by QKD over a line with small transmission probability η , a limit known as ‘repeaterless secret key capacity’ (SKC₀) or PLOB bound [3]. Quantum repeaters offer a theoretical solution to extend the range of QKD [5–8]. However, a full-fledged quantum repeater remains outside the reach of present technology, due to the difficulty in building and reliably operating a low-loss quantum memory. A partial implementation of a memory-assisted repeater has been recently achieved [9] in the form of measurement-device-independent QKD [10] (see also [11]).

An alternative method to extend the transmission range of QKD without using a quantum memory has been recently discovered and named ‘twin-field’ (TF) QKD [12] due to the peculiar interference between two fields that have related, though not necessarily identical, optical phase. The secret key rate (SKR) of TF-QKD

scales proportionally to $\sqrt{\eta}$, similar to a quantum repeater with a single node, thus entailing a major increase in the SKR-vs-distance figure of QKD. This has led to the realisation of several experiments that display formidable long-range (or high-loss) characteristics [13–18].

The security of the original TF-QKD protocol was first proved in [12] for a limited class of attacks and then extended to general attacks in [19] and [20]. Soon after, its experimental implementation was also considerably simplified thanks to protocol variants that waived the need for phase randomisation and reconciliation for signal states [21–26]. The ‘phase-matching’ protocols [21–23] feature signal states with a constant global phase while the ‘sending’ or ‘not-sending’ protocol (SNS) [24–26] encode qubits upon optical pulses with random and unknown phases. With the help of ‘two-way classical communication’ (TWCC) [27, 28], the SNS protocol is able to remove the quantum bit error rate (QBER) floor intrinsic to the encoding method thereby extending the communication distance [29]. By running the TWCC protocol over ultralow-loss (ULL) optical fibres, a distance of 509 km has been achieved [18], which represents the current record distance for secure quantum communications over optical fibres.

RESULTS

Dual-band phase stabilisation

In order to perform TF-QKD, it is necessary to compensate the phase drift of the encoded pulses interfering in the intermediate node (Charlie) after travelling through hundreds of kilometres in fibre. The typical phase drift for a 100 km fibre was measured to exceed 1000 rad/s [12]. Active compensation of rapid drift requires bright reference light to be transmitted in the same fibre along with the quantum signals for phase calibration. The longer the fibre, the brighter the reference pulses have to be, as phase calibration requires a minimum power level to be received at the detectors. So far, all the TF-QKD experiments used the same wavelength for both quantum and reference signals, with the help of time-divisional modulation to achieve the necessary intensity contrast. However, this approach ceases to work for ultralong fibres. The ever-increasing intensity of the reference pulses causes a strong Rayleigh scattering that travels back and forth along the fibre and dramatically reduces the quantum signal to noise ratio. As proven in [18], the noise due to double Rayleigh backscattering becomes comparable with the dark counts noise of Charlie’s detectors around 500 km of ultralow-loss fibre. Moreover, the performance of a system using a single wavelength for both dim and bright signals will be inevitably limited by the finite dynamic range of the detectors. These two aspects fundamentally limit ‘single-band’ TF-QKD.

In this work, we adopt a novel ‘dual-band’ phase control using two wavelengths multiplexed on a single fibre, which as well as solving the phase stabilisation problem in TF-QKD, could have broad applicability in a range of optical applications that require space-separated phase control. The technique allows strong intensity contrast between reference and quantum signals while the wavelength separation prevents the Rayleigh scattering from contaminating the quantum signals. An active phase compensation of the intense reference light leads to an immediate reduction of the phase drift by more than a factor 1000, allowing the residual drift to be compensated at a much slower pace using light signals that have comparable intensity and identical wavelength as the quantum signals. It is worth noticing that the two wavelengths are generated by independent lasers and are not phase-locked, i.e., the stabilisation mechanism works also without an exact phase relation between the two bands. This counter-intuitive detail is fundamental to guarantee the practicality of the setup, which makes ultra-stable cavities or complex light modulation schemes unnecessary.

The resulting setup is versatile, capable of implementing all kinds of TF-QKD protocols proposed so far, including the phase-matching ones [21–23], which cannot be efficiently run without an active phase stabilisation method. With this setup, clocked at 1 GHz, we run various protocols and achieve record SKRs and distances for secure quantum communications over optical fibres. The

SKR overcomes the absolute SKC_0 at several distances, thus proving the quantum repeater-like behaviour of our system. In addition to estimating the SKR, we also extract, for the first time, actual raw bits from a TF-QKD protocol. This is a necessary requisite for a system that aims to distribute secure cryptographic keys to remote users in a real-world scenario.

Setup

The experimental setup (Fig. 1) is composed of three modules. The modules of Alice and Bob, who are the communicating users, transmit their quantum signals to Charlie’s module via the quantum channel, made of spools of Corning SMF-28 ULL fibre. The spools are spliced into different sets, thus enabling experiments over 5 different communication distances, ranging from 153.2 to 605.2 km. The average loss coefficient of the fibre channel, including splices and connectors, is 0.171 dB/km. For detailed information on the fibre properties, refer to Table II in the Supplementary Material.

The setup uses two wavelengths: λ_1 (1550.12 nm) and λ_2 (1548.51 nm), disseminated by Charlie’s L1 and L2 lasers over long servo fibre links. Each servo link spans 305.7 km of standard single mode fibre, giving a total separation between the two communicating users exceeding 611 km. To ensure sufficient power arriving at each user, two erbium-doped fibre amplifiers (EDFAs) are placed in each servo link to compensate for channel losses: one EDFA is placed mid-span and the other is just before the entrance to Alice/Bob. Despite the long distance and periodic amplification, we verified the absence of detrimental nonlinear optical effects (i.e., stimulated Brillouin scattering, four-wave mixing etc.).

The users’ local lasers ($L1_A$ and $L1_B$) have a free running linewidth of 50 kHz. They are locked to the disseminated λ_1 signal through an optical phase-locked loop (OPLL), and generate light for encoding dim quantum signals. The encoders in the users’ stations operate at 1 GHz, and they carve the λ_1 input light into a train of 250 ps pulses. The even-numbered pulses are modulated in intensity and phase, according to the requirements of the different TF-QKD protocols to be implemented. We refer to these as ‘quantum signals’. The odd-numbered pulses do not receive any further modulation and are used to track the phase drift of the quantum signals. Hence, we refer to them as ‘dim reference’. All pulses are attenuated to the single-photon level before entering the quantum channel. A step-by-step description of the encoder modulation is given in the Methods. The disseminated λ_2 signal is routed via dense wavelength division multiplexing (DWDM) within users’ modules for transmitting to Charlie together with the quantum signal.

Alice and Bob provide independent pre-compensation of the polarisation rotation of the signals at the two wavelengths so that all photons arrive with identical polarisation at Charlie’s receiving 50/50 beam splitter (for more details on this aspect refer to Sec. III of the Supplementary Material). The interference output at the beam splitter are separated by DWDM filters before detec-

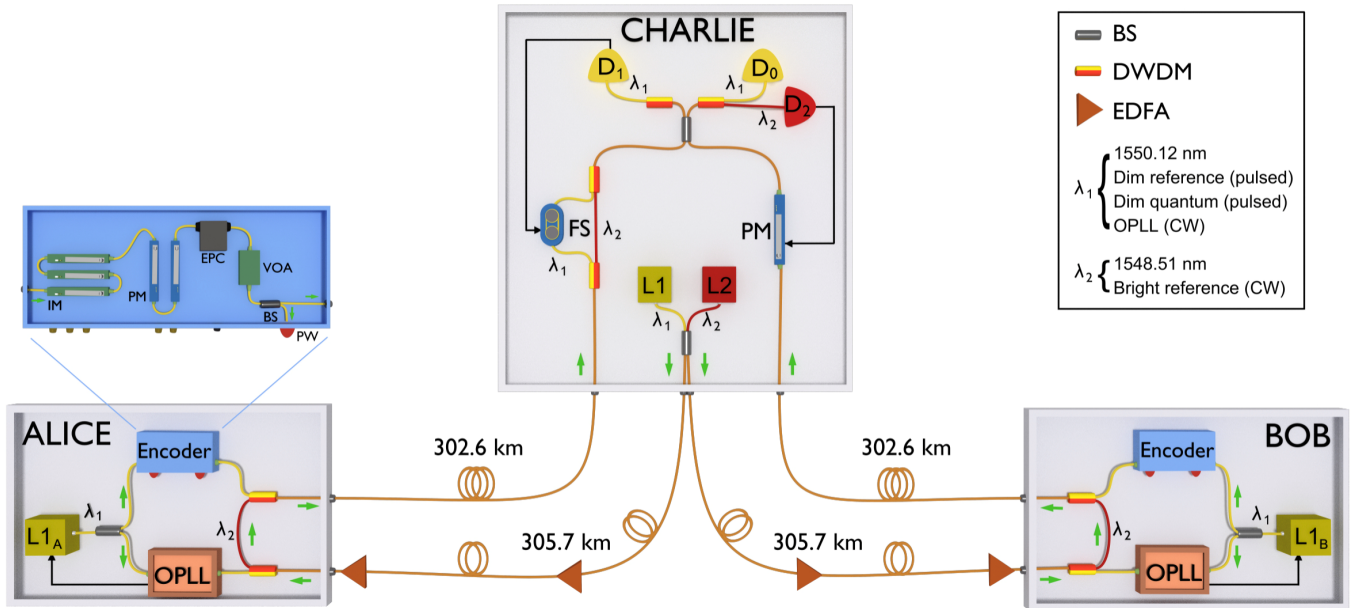


FIG. 1. **Experimental setup.** Charlie's L1 (λ_1) and L2 (λ_2) lasers provide continuous-wave signals for wavelength dissemination and phase tracking, respectively. Combined via a beam splitter (BS), they are transmitted to the symmetric users (Alice and Bob) over long servo links (305.7 km in each arm) equipped with periodic erbium doped fibre amplifiers (EDFAs). Each user owns an optical phase-locked loop (OPLL) to clone the λ_1 wavelength to their local lasers (L1_A and L1_B). The cloned output is encoded before being wavelength multiplexed with the disseminated λ_2 light into the quantum channel. Alice and Bob's signals meet at Charlie's second BS and interfere. Detectors D₀ and D₁ record the interference output for λ_1 , while D₂ records the one for λ_2 . The dual band phase stabilisation realised by a phase modulator (PM) and a fibre stretcher (FS) removes fast and slow phase drifts respectively. **Encoder boxes.** A set of intensity and phase modulators inside each user's Encoder allow them to run different TF-QKD protocols. IM: intensity modulator, EPC: electrical polarisation controller, VOA: Variable optical attenuator, PW: Power meter, DWDM: dense wavelength division multiplexer/demultiplexer.

tion by three superconducting nanowire single photon detectors (SNSPD's): D₀ and D₁ for λ_1 photons and D₂ for λ_2 photons. Charlie's module further contains a phase modulator (PM) in one input arm and a fibre stretcher (FS) sandwiched between a pair of DWDMs in the other arm. Full stabilisation of the quantum signal is achieved in two steps (a block diagram representation of the feedback systems is reported in Fig. 2 of the Supplementary Material), each step using a specific wavelength of the dual-band stabilisation. First, Charlie measures the bright reference and uses a field programmable gate array (FPGA) with an integrated counter to apply a proportional-integral-differential (PID) control to the bias of his PM. The brightness of the signal detected by D₂ allows this control loop to operate at 200 kHz, sufficient to stabilise the phase drift caused by the long fibre channels. Since λ_1 and λ_2 are spectrally close and travel along the same fibre between the users and the central node, the λ_2 light can be used to stabilise the phase of the pulses at λ_1 . Assuming unidirectional phase drift, the λ_2 -stabilisation will reduce the phase drift in λ_2 by approximately $\lambda_1/|\lambda_2 - \lambda_1| \approx 1000$. In the real scenario, the non-unidirectionality of the phase drift makes the actual reduction even greater, as we will show later. The slowed drift can then be comfortably corrected through a second PID controller adjusting the bias of the FS at

a rate of 10-20 Hz, without requiring an intense input signal. The input signal for this feedback is provided by the interference outcome of the dim reference pulses at λ_1 recorded by D₁. More information about the feedback systems and on the sources of the residual slow drift is provided in the Methods.

Experimental Results

Figure 2 shows the interference outcome for λ_1 , over a 605 km long quantum channel, at different stages of the stabilisation process. The purple dots in Fig. 2a represent the interference when no phase stabilisation is applied. At this distance, the free drift is so rapid (in the order of 10^4 rad/s) that it is impossible to discern any interference fringe over a 1 s time scale. Only on a millisecond time scale (Fig. 2b) we can distinguish the interference fringes. The phase drift rate distribution associated with this measurement is shown in the purple histogram in Fig. 2c. Its standard deviation allows us to quantify the phase drift in $11.89 \cdot 10^3$ rad/s.

After activating the stabilisation from λ_2 , the phase drift rate for λ_1 reduces drastically (see orange points in Fig. 2a). It is now possible to follow the evolution of constructive or destructive interference over a time scale of tens of seconds. The effectiveness of this stabilisation is quantifiable by the reduction in the phase drift

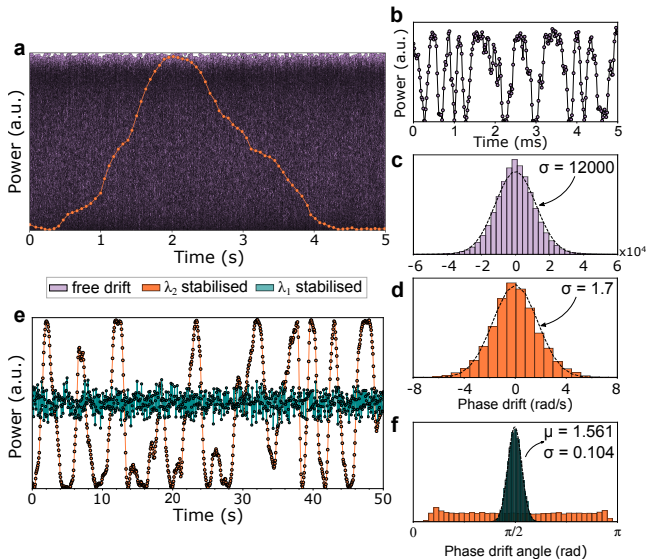


FIG. 2. **Dual-band stabilisation.** Data in this figure shows the interference of λ_1 light at different stabilisation stages. Data was acquired over 605 km quantum and 611 km servo fibres, in a configuration identical to that in Fig. 1 except Encoder boxes were bypassed. Detector D_1 (Fig. 1) was used to record the data. The colour code is: purple for free drift, orange for λ_2 -stabilised data and teal for λ_1 -stabilised data. **a**, Comparison between free drifting and λ_2 -stabilised data. Integration times were 20 μ s and 60 ms for free drifting and λ_2 -stabilised data, respectively, due to the different time scales. An interference visibility measurement over the free drifting (λ_2 -stabilised) data yields 98.22% (96.24%). **b**, Same data set as in (a) but over a ms time scale. **c**, Histogram of the free drifting phase drift. The standard deviation is 11890 rad/s. **d**, Histogram of the λ_2 -stabilised phase drift. The standard deviation is 1.74 rad/s, i.e. about 6800 times smaller than in sub-figure (c). **e**, Comparison between λ_2 -stabilised data (orange) and data stabilised using both wavelengths, λ_1 and λ_2 (teal). **f**, Phase offset distributions for the data shown in (e). λ_2 -stabilised data has an almost uniform distribution over $[0, \pi]$ whereas λ_1 -stabilised data has a distribution peaked around $\pi/2$.

rate for the recorded data (orange histogram in Fig. 2d). When feedback from the bright reference at λ_2 is enabled, the standard deviation of the drift rate decreases to 1.74 rad/s, a value ~ 6800 times smaller than without the bright reference stabilisation. This reduction is considerably better than the estimated factor 1000 due to the cancellation of rapid opposite drifts. The residual slow phase drift of λ_1 can be readily compensated by using the dim reference pulses at this wavelength, which leads to a stable interference output (teal dots in Fig. 2e). Figure 2f shows the phase distribution between the interfering λ_1 signals locked to have $\pi/2$ difference. The locking error is only 0.10 rad (standard deviation of the teal coloured distribution in the figure), which contributes to the QBER by approximately 2%.

Using the described dual-band stabilisation, we performed four experiments with different TF-QKD pro-

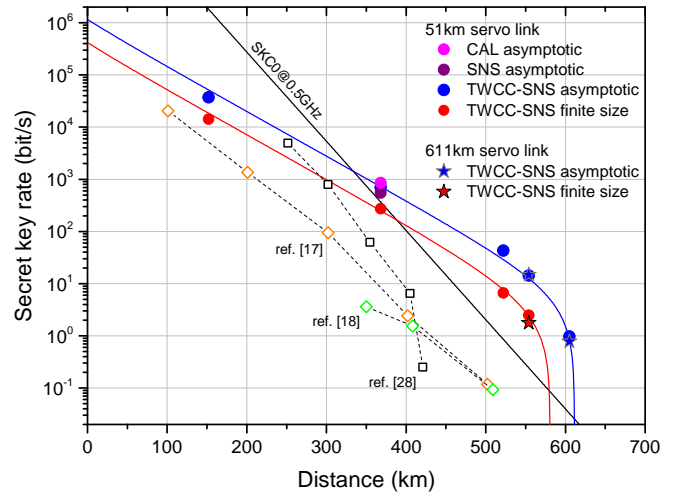


FIG. 3. **Key rate simulations and results.** Secret key rates are plotted against the quantum channel length. This is constituted by ultra-low loss (ULL) fibres of 0.171 dB/km loss. The SKC_0 bound for unitary detection efficiency (black line) is plotted along the simulations for the TWCC SNS TF-QKD protocol in the asymptotic and finite size regimes (blue and red curves respectively). Filled markers show the experimental results we obtained for the different protocols whereas unfilled markers are the state-of-the-art results in term of SKR over distance for fibre-based TF-QKD [17, 18] (diamonds) and QKD [30] (squares).

ocols, varying the operational regimes and optimising the parameters in each case. Firstly, the CAL [22] and SNS [24] protocols in the asymptotic regime, then the SNS with the TWCC method [29], both in the asymptotic and in the finite-size regimes [25, 26]. In the practically relevant case of finite-size TWCC-SNS, we also extracted real bits of the raw key. We performed these experiments in two stages. First, we developed a simplified asymmetric setup to assess the feasibility of long-distance TF-QKD with dual-band phase stabilisation, featuring a single OPLL and a 51 km servo fibre. We then moved on to a symmetrical configuration where the frequency reference is disseminated by Charlie (Fig. 1) via 611 km servo fibre for the final experiments over the two longest quantum channel fibre distances. Details about the asymmetric experimental setup, the protocol parameters, together with additional information on the patterns used for encoding, are given in Sec. I and V of the Supplementary Material.

In Fig. 3 we report our results in terms of SKR versus distance, together with the simulation curves and the state-of-the-art SKRs for long-distance TF-QKD [17, 18] and QKD [30] over optical fibres. In the same graph we also plot the absolute SKC_0 , which assumes ideal equipment for Alice and Bob and hence is the most difficult bound to overcome. Surpassing this limit proves the repeater-like behaviour of our setup. The complete experimental results can be found in Sec. VI of the Supplementary Material. The CAL and SNS protocols

have been implemented on a 368.7 km-long optical fibre (62.8 dB loss) and analysed in the asymptotic scenario. For CAL, we obtain an SKR of 852.7 bit/s, 2.39 times larger than SKC_0 . For SNS, the SKR is 549.2 bit/s, 1.54 times larger than SKC_0 .

Using the TWCC SNS version of TF-QKD, we take measurements at 153.3, 368.7, 522.0, 555.2 and 605.2 km, i.e., from 26.5 dB to 104.8 dB loss, and we extract positive SKRs both in the asymptotic and in the finite-size regimes. In Fig. 3, blue (red) symbols refer to the experimental results obtained in the asymptotic (finite-size) case scenario. Stars (dots) represent results obtained through the symmetric (asymmetric) setup with a 611 km (51 km) servo fibre. Despite periodic optical amplifications, the longer servo link introduces only a marginal reduction of the secret key rate. At a 555 km quantum channel and a 611 km servo link, with less than 2 h of continuous measurement, we are able to extract a finite-size SKR of 1.777 bit/s, a value 7.68 times higher than the absolute SKC_0 . Extending the quantum channel to 605.2 km, with a loss budget of 104.8 dB, we achieve an asymptotic SKR of 0.778 bit/s, which is 24 times higher than the SKC_0 . This represents the first fibre-based secure quantum communication beyond the barriers of 600 km and 100 dB.

To further appreciate the progress entailed by our new technique, we compare our results with the experimental points setting the current record distances for fibre-based QKD (421 km [30]) and TF-QKD (502 km [17], 509 km [18]). Distance-wise, there is an increase of tens of (more than a hundred) kilometres over TF-QKD (QKD) prior art. The main element enabling the distance improvement over previous TF-QKD implementations is the dual-band stabilisation technique, which leads to negligible contamination of the encoded signal by the bright reference. In previous experiments, the bright stabilisation signal was emitted at the same wavelength as the encoded signal, thus causing an intense double Rayleigh backscattering that ultimately limited the maximum communication distance. In our case, on the other hand, even at the longest distance the noise introduced by the stabilisation signal was below the detectors' dark counts.

The dual-band stabilisation technique leads also to an even more pronounced enhancement of the SKR, with an improvement of 2 orders of magnitude at 500 km, the furthest distance achieved by prior art. This is possible because we could keep the clock rate of the encoded signals at the high value of 500 MHz at all distances. In previous experiments, where the stabilisation signal was time-multiplexed, the protocol clock rate had to be reduced considerably to accommodate for reference signals, and to leave some recovery time at the detectors (after these received the bright intensity reference pulses).

All the TF-QKD experiments performed so far, as well as the vast majority of long-distance QKD experiments, have only provided an in-principle estimation of the SKR without a real extraction of the bits that form a crypto-

graphic key after suitable post-processing. In our experiment, we extract real strings of bits from the SNS protocol and process them with the TWCC method. The generation of raw bits is a challenging task, especially with a clock rate as high as 1 GHz, as it requires individual tagging and real-time manipulation of the signals recorded at the detectors. Figure 4 gives a graphical representation of the TWCC method applied to a raw bit string extracted during the experiment performed at 522 km. The bits of the strings are displayed as white or black pixels depending on their value 0 or 1, respectively. The leftmost and central panels in the first row show Alice's and Bob's raw strings, distilled from the SNS protocol, whereas the rightmost panel reports the bitwise addition of the two strings. The density of the dots in the first two panels reveal a slight bias (53.8%) in the bit value which is intrinsic to the SNS protocol [24]. A simulation shows that with our parameters a bias of 52.7% has to be expected. On the other hand, the black dots in the rightmost panel highlight the conflicting bits in the users' raw keys, which amount to a 16% of the total. The second row of Fig. 4 shows the effect of TWCC on the users' strings. TWCC induces a considerable reduction of the errors, from 16% to 3.5%, and of the bias in the strings at the expenses of the strings length, which decreases by $\sim 70\%$. However, the overall effect of TWCC is beneficial, as it increases the signal-to-noise ratio of the raw keys and so also the range of TF-QKD.

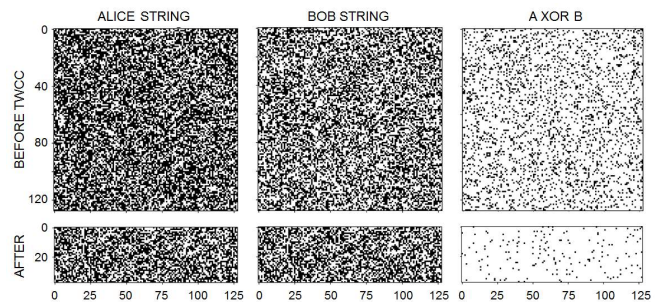


FIG. 4. **Binary maps of the extracted bit strings.** Samples of the bits extracted from the experiment performed at 522 km before (top panels) and after (bottom panels) TWCC is applied. *Top:* The first two squares on the left (128×128 pixels) are a sample of the users' raw strings before TWCC is applied, with white (black) pixels associated with the bit value 0 (1). The third square on the right is obtained by modulo-2 addition (XOR) of the first two. The black dots in this square represent the errors in the strings. *Bottom:* Refined keys after TWCC has been applied. The strings shrink by 70% into rectangles with 128×38 pixels. Reduction in key size is accompanied by a substantial reduction in the key errors, as is apparent from the rightmost rectangle.

We have shown that dual-band phase stabilisation can dramatically reduce the phase fluctuations on optical fibre by almost four orders of magnitude. This has allowed us to overcome the fundamental noise limitation of long distance TF-QKD and increase its secret key rate from the current millibit per second range to the bit per second range for the longest fibre length. We notice here that 1 bit/s key generation rate is sufficient to enable fast key refresh of symmetric cryptographic protocols, such as AES, several times per day. Our setup tolerates a maximum loss beyond 100 dB allowing quantum communication over 600 km of fibre for the first time. We believe these techniques will have more general application in quantum communications, for example enabling DLCZ-type quantum repeaters [6], longer-baseline telescopes [31], quantum fingerprint [32–34] over longer distances or a phase-based architecture for the quantum internet [35].

Note added - During the completion of our work, one of the anonymous referees noted that the finite-size equations we borrowed from Refs. [25, 26] only hold if the variables are i.i.d., a result not known at the time of writing. A full analysis of this point has only recently appeared in a preprint [36] and suggests that the removal of the i.i.d. assumption only entails a slight increase in the failure probability of the protocol.

We thank Xiang-Bin Wang and Hai Xu for their useful feedback on the TWCC protocol. The authors acknowledge funding from the European Union’s Horizon 2020 research and innovation programme under the grant agreement No 857156 “OPENQKD” and under the Marie Skłodowska-Curie grant agreement No 675662. M.M. acknowledges financial support from the Engineering and Physical Sciences Research Council (EPSRC) and Toshiba Europe Ltd.

Author contributions. M.P. and M.M. developed the experimental set-up, performed the measurements and analysed the data. M.S. and R.I.W. supported the experimental work. M.-J.L. provided the ultralow-loss fibres. Z.L.Y., M.L. and A.J.S. guided the work. M.L., M.P. and M.M. provided the simulations and wrote the manuscript, with contributions from all the authors.

Competing interests. The authors declare no competing interests.

Data availability. The data that support the plots within this paper and other findings of this study are available from the corresponding authors on reasonable request.

Code availability. The codes used to process the data for this paper are available from the corresponding authors on reasonable request.

Correspondence and requests for materials. should be addressed to M.P. and M.L.

-
- [1] Bennett, C. H. & Brassard, G. Quantum cryptography: Public key distribution and coin tossing. *Theor. Comput. Sci.* **560**, 7–11 (2014).
 - [2] Ekert, A. K. Quantum cryptography based on Bell’s theorem. *Phys. Rev. Lett.* **67**, 661–663 (1991).
 - [3] Pirandola, S., Laurenza, R., Ottaviani, C. & Banchi, L. Fundamental limits of repeaterless quantum communications. *Nat. Commun.* **8**, 15043 (2017).
 - [4] Takeoka, M., Guha, S. & Wilde, M. M. Fundamental rate-loss tradeoff for optical quantum key distribution. *Nat. Commun.* **5**, 5235 (2014).
 - [5] Briegel, H.-J., Dür, W., Cirac, J. I. & Zoller, P. Quantum repeaters: The role of imperfect local operations in quantum communication. *Phys. Rev. Lett.* **81**, 5932–5935 (1998).
 - [6] Duan, L.-M., Lukin, M. D., Cirac, J. I. & Zoller, P. Long-distance quantum communication with atomic ensembles and linear optics. *Nature* **414**, 413–418 (2001).
 - [7] Sangouard, N., Simon, C., de Riedmatten, H. & Gisin, N. Quantum repeaters based on atomic ensembles and linear optics. *Rev. Mod. Phys.* **83**, 33–80 (2011).
 - [8] Guha, S. *et al.* Rate-loss analysis of an efficient quantum repeater architecture. *Phys. Rev. A* **92**, 022357 (2015).
 - [9] Bhaskar, M. K. *et al.* Experimental demonstration of memory-enhanced quantum communication. *Nature* **580**, 60–64 (2020).
 - [10] Lo, H.-K., Curty, M. & Qi, B. Measurement-device-independent quantum key distribution. *Phys. Rev. Lett.* **108**, 130503 (2012).
 - [11] Braunstein, S. L. & Pirandola, S. Side-channel-free quantum key distribution. *Phys. Rev. Lett.* **108**, 130502 (2012).
 - [12] Lucamarini, M., Yuan, Z. L., Dynes, J. F. & Shields, A. J. Overcoming the rate-distance limit of quantum key distribution without quantum repeaters. *Nature* **557**, 400–403 (2018).
 - [13] Minder, M. *et al.* Experimental quantum key distribution beyond the repeaterless secret key capacity. *Nat. Photonics* **13**, 334–338 (2019).
 - [14] Wang, S. *et al.* Beating the fundamental rate-distance limit in a proof-of-principle quantum key distribution system. *Phys. Rev. X* **9**, 021046 (2019).
 - [15] Liu, Y. *et al.* Experimental twin-field quantum key distribution through sending or not sending. *Phys. Rev. Lett.* **123**, 100505 (2019).
 - [16] Zhong, X., Hu, J., Curty, M., Qian, L. & Lo, H.-K. Proof-of-principle experimental demonstration of twin-field type quantum key distribution. *Phys. Rev. Lett.*

- 123**, 100506 (2019).
- [17] Fang, X.-T. *et al.* Implementation of quantum key distribution surpassing the linear rate-transmittance bound. *Nature Photonics* **14**, 422–425 (2020).
- [18] Chen, J.-P. *et al.* Sending-or-not-sending with independent lasers: Secure twin-field quantum key distribution over 509 km. *Phys. Rev. Lett.* **124**, 070501 (2020).
- [19] Tamaki, K., Lo, H.-K., Wang, W. & Lucamarini, M. Information theoretic security of quantum key distribution overcoming the repeaterless secret key capacity bound. *arXiv:1805.05511* (2018).
- [20] Ma, X., Zeng, P. & Zhou, H. Phase-matching quantum key distribution. *Phys. Rev. X* **8**, 031043 (2018).
- [21] Lin, J. & Lütkenhaus, N. Simple security analysis of phase-matching measurement-device-independent quantum key distribution. *Phys. Rev. A* **98**, 042332 (2018).
- [22] Curty, M., Azuma, K. & Lo, H.-K. Simple security proof of twin-field type quantum key distribution protocol. *npj Quantum Information* **5**, 64 (2019).
- [23] Cui, C. *et al.* Twin-field quantum key distribution without phase postselection. *Phys. Rev. Applied* **11**, 034053 (2019).
- [24] Wang, X.-B., Yu, Z.-W. & Hu, X.-L. Twin-field quantum key distribution with large misalignment error. *Phys. Rev. A* **98**, 062323 (2018).
- [25] Jiang, C., Yu, Z.-W., Hu, X.-L. & Wang, X.-B. Unconditional security of sending or not sending twin-field quantum key distribution with finite pulses. *Phys. Rev. Applied* **12**, 024061 (2019).
- [26] Yu, Z.-W., Hu, X.-L., Jiang, C., Xu, H. & Wang, X.-B. Sending-or-not-sending twin-field quantum key distribution in practice. *Sci. Rep.* **9**, 3080 (2019).
- [27] Gottesman, D. & Lo Hoi-Kwong. Proof of security of quantum key distribution with two-way classical communications. *IEEE Trans. Inf. Theory* **49**, 457–475 (2003).
- [28] Chau, H. F. Practical scheme to share a secret key through a quantum channel with a 27.6% bit error rate. *Physical Review A* **66**, 802 (2002).
- [29] Xu, H., Yu, Z.-W., Jiang, C., Hu, X.-L. & Wang, X.-B. Sending-or-not-sending twin-field quantum key distribution: Breaking the direct transmission key rate. *Phys. Rev. A* **101**, 042330 (2020).
- [30] Boaron, A. *et al.* Secure quantum key distribution over 421 km of optical fiber. *Phys. Rev. Lett.* **121**, 190502 (2018).
- [31] Gottesman, D., Jennewein, T. & Croke, S. Longer-baseline telescopes using quantum repeaters. *Phys. Rev. Lett.* **109**, 070503 (2012).
- [32] Arrazola, J. M. & Lütkenhaus, N. Quantum fingerprinting with coherent states and a constant mean number of photons. *Phys. Rev. A* **89**, 062305 (2014).
- [33] Xu, F. *et al.* Experimental quantum fingerprinting with weak coherent pulses. *Nat. Commun.* **6**, 8735 (2015).
- [34] Zhong, X., Xu, F., Lo, H.-K. & Qian, L. Efficient experimental quantum fingerprinting with wavelength division multiplexing. *arXiv:2005.06049v1* (2020).
- [35] Kimble, H. J. The quantum internet. *Nature* **453**, 1023–1030 (2008).
- [36] Jiang, C., Hu, X.-L., wen Yu, Z. & bin Wang, X. Composable security for practical quantum key distribution with two way classical communication. *arXiv:2102.00739v1* (2021).
- [37] Lo, H.-K., Ma, X. & Chen, K. Decoy state quantum key distribution. *Phys. Rev. Lett.* **94**, 230504 (2005).
- [38] Wang, X.-B. Beating the photon-number-splitting attack in practical quantum cryptography. *Phys. Rev. Lett.* **94**, 230503 (2005).

METHODS

Encoder boxes. For a detailed representation of the components inside the encoder boxes see inset diagram in Fig. 1. The incoming CW light arrives already aligned in polarisation with the optical axes of the subsequent modulators. The first components in the encoders are three intensity modulators (IMs), used to carve 250 ps long pulses at a 1 GHz rate, with three possible intensity levels (u , v , w). The intensity ratios between the different intensity levels can be adjusted by the AC amplitude driving the IMs.

Two phase modulators (PMs) are then used to encode the phase of the optical pulses. In this system, we cascade two PMs instead of using just one to reduce their RF signal amplitudes. Limiting each PM to a modulation range of $[-\frac{\pi}{2}, \frac{\pi}{2}]$, we achieve a phase modulation that covers the whole $[0, 2\pi)$ range and that is linear with its driving signals amplitude. Each PM is driven by a 8-bit DACs, and with two cascaded we are able to encode 512 different phase values over the 2π phase range.

All the modulators are driven by two synchronised 12 GSa/s waveform generators, one for each user, programmed to encode a 25040-pulse long pseudo-random pattern. For more information on the encoded pattern refer to Sec. VI of the Supplementary Material.

The PMs are followed by an electrically driven polarisation controller (EPC), a variable optical attenuator (VOA), and a 99:1 beam splitter (BS). The EPC is used to control the polarisation of the λ_1 photons after transmission through the channel. Each user has a continuous polarisation optimisation routine that aligns the quantum signals along the preferred optical axis at Charlie.

The VOA sets the flux of the quantum signal before injection into the quantum channel, through a flux calibration control loop that continuously adjusts the VOA so as to have a stable optical output, monitored at the strong output of the BS.

Feedback systems. The dual-band phase-stabilisation strategy employed in this experiment enabled us to stabilise the quantum channel without affecting the encoding in the wavelength reserved for the quantum signal (λ_1) or the clock rate of the protocol, which was kept at 500 MHz at all the tested distances. Its general design is presented in Fig. 1 and its detailed block diagram is given in Fig. 2 of the Supplementary Material.

There, Fig. 2a shows the stabilisation method based on the bright reference at λ_2 . It features a closed loop cycle that locks the interference between Alice’s and Bob’s bright reference beams to a given intensity level. This, in turn, locks the phase offset between these signals to a fixed value. The bright reference interference is monitored by the SNSPD D_2 . Single photons detected by D_2 are integrated over a period of 5 μ s. The difference between the integrated number of counts and the set value, constitutes the error signal of a PID controller implemented with an FPGA clocked at 200 kHz. By tuning the DC offset of a phase modulator (PM) that acts on the light coming from Bob, the FPGA controls the interference between the bright references. It is important to notice here that the phase shift applied by the PM affects both the wavelengths λ_2 and λ_1 . The feedback based on λ_2 fully stabilises the bright reference light while it only partially stabilises the quantum one.

The remaining (slow) phase drift on λ_1 is related to two

factors: the fact that λ_1 and λ_2 travel separately in certain sections of the setup (necessary for the protocol encoding over λ_1 at the transmitting stations), and the fact that the fast feedback introduces a phase drift over λ_1 when the length difference between the two channels varies over time. The former component of the slow phase drift can be seen as the phase noise picked up by an asymmetric Mach-Zender interferometer having the dimensions of those sections of the setup where the two wavelengths travel separately. The latter component can be explained as a consequence of the finite range of the PM, and of the phase locking of the fast feedback over λ_2 , rather than λ_1 .

The PM in the fast feedback actively compensates the fast phase drift. However, its finite adjustment range is incapable of compensating at entirety the phase drift caused by fibre length variation. It must rely on multiple (M) resets in order to maintain the λ_2 phase difference to $\phi = 2\pi M + \phi_t$, where ϕ_t is the target phase. Due to the $\lambda_2 - \lambda_1$ wavelength difference, this compensation will introduce a residual phase drift ($\Delta\phi$) over λ_1 equal to:

$$\Delta\phi = 2\pi M \cdot \left(\frac{\lambda_2 - \lambda_1}{\lambda_1} \right). \quad (1)$$

The residual drift introduced by the λ_2 -stabilisation over λ_1 is estimated to be $\frac{\phi}{\Delta\phi} = \frac{\lambda_1}{\lambda_2 - \lambda_1} \approx 1000$ times smaller than the original fibre phase drift, if assuming unidirectional fibre length drift. In reality, the fibre length drift direction is random. With cancellation of positive and negative 2π resets, we obtain experimentally a higher reduction factor of ~ 6800 (as shown in Fig. 2).

Supplementary Material Fig. 2b shows the stabilisation mechanism that corrects the residual phase drift on λ_1 . The error signal for it is provided by the overall interference of quantum signals and dim reference. The quantum signals are interleaved with the dim reference pulses, which are unmodulated and have the same intensity as the brightest decoy pulse (u). The presence of dim reference pulses guarantees that the averaged output of the interference is directly related to the residual phase offset in λ_1 . This is retrieved by integrating the single photons detected by SNSPD D_1 over 50 ms or 100 ms, depending on the distance. The difference between this value and a set value provides the error signal for a PID controller implemented with a micro-controller operating at the frequency of 20 Hz or 10 Hz, depending on the distance. The micro-controller corrects the phase offset by modulating a fibre stretcher acting on the quantum signal coming from Alice. Differently from the stabilisation in λ_2 , the one in λ_1 acts solely on the quantum signals and can therefore correct its residual phase drift.

Due to the different expansion/contraction rates of the channels connecting Charlie to the two users, during the protocol execution we had to compensate for the change in length of the quantum channels. We did that by opportunely delaying the pattern encoding of one user with respect to the other, aiming at obtaining always optimal time alignment of the users’ pulses at Charlie’s BS. The intervals between these alignment adjustments depended on the stability of the environmental conditions in the lab, and varied from once every 4 minutes, up to once every of 30 minutes. From the highest adjustments frequency, we estimated an upper limit of the length difference drift between the two sides of the communication channel (in our air-conditioning temperature stabilised lab) of ~ 3 mm/min in the longest experimental setting.

Protocols. To demonstrate the multi-protocol aspect of our system, we implemented different variants of TF-QKD, in different regimes. We list them as CAL [22], SNS [24–26] and TWCC-SNS [29]. Their detailed description and security proofs can be found in the referenced papers. See also Methods in [13]. Here we describe our encoding method and the equations used to extract the secret key rate from each protocol.

In all protocols, we consider a symmetric situation, with identical photon fluxes for the users Alice and Bob. This is the real situation in the experiment, where fibre lengths and losses between the users and Charlie are nearly identical (see e.g. Table II in Supplementary Material). Therefore we only describe the relevant steps for the user Alice; Bob will execute similar operations in his own location. During the preparation stage, Alice generates weak coherent states of the form $|\sqrt{\mu}e^{i\theta}\rangle$. She randomly selects a basis X or Z with probabilities P_X or P_Z ($P_X + P_Z = 1$). If she chooses X (test basis), she randomly selects a flux value $\mu = \{u, v, w\}$ with conditional probability $P_{\mu|X} = \{P_{u|X}, P_{v|X}, P_{w|X}\}$, $P_{u|X} + P_{v|X} + P_{w|X} = 1$, and a random global phase value $\phi \in [0, 2\pi)$. She then prepares and send the phase-randomised weak coherent state $|\sqrt{\mu}e^{i\phi}\rangle$. If she chooses Z (code basis), she randomly selects a bit value $\alpha = \{0, 1\}$ and sets the photon flux to $\mu = \{s, n\}$ with conditional probability $P_{\mu|Z} = \{P_{s|Z}, P_{n|Z}\}$, $P_{s|Z} + P_{n|Z} = 1$. In CAL, bits are encoded as coherent states $|\sqrt{s}e^{i\alpha\pi}\rangle$. In SNS, bits are encoded on the photon flux, with s (n) representing a bit value 1 (0) for Alice and a bit value 0 (1) for Bob. With our encoder, the photon fluxes w and n are both very small, in the order of 10^{-4} . Therefore sending out a photon flux n , or w , is equivalent by all practical means to not sending out any flux at all. We denote the probability of ‘not sending’ conditional on choosing the Z basis as $P_{n|Z}$ and the probability of sending a photon flux s conditional on the Z basis as $P_{s|Z}$ or simply ϵ . The detailed values of the parameters used in the experiment depend on the protocol (CAL, SNS, TWCC) and on the regime (asymptotic or finite-size) adopted. They are listed in Tables III and IV in the Supplementary Material.

After the preparation stage, Alice and Bob send their pulses to central node, Charlie. Charlie should interfere the received pulses on a beam splitter and measure the result, announcing publicly which detector click. If Charlie is malicious and adopts a different detection and announcement strategy the security of TF-QKD remains unaffected. After a total of N_0 signals have been sent, the quantum transmission is over and Charlie publicly announces his measurements. When Charlie’s announcement is complete, the users announce their bases. For the X basis, they also disclose their intensities μ and, limitedly to the SNS protocol, they announce the values of their global phases ϕ . Alice and Bob post-select the events for which they used matching bases and intensities. For SNS, they also select the events with global phase values not mismatched by more than Δ modulo π . The users extract the bits from the Z basis events and use the X basis events to perform the security analysis. In TWCC, the bits in the string distilled from the Z basis are randomly paired and bit-wise XOR-ed. More specifically, Bob randomly pairs the bits up and announces the positions and parities of each pair. Alice uses this information to repeat this step with her own string and announces the instances for which her parity calculation matches Bob’s one. The users will discard both bits in the pair if the announced parities are different. If the

parities are the same, the users keep the first bit of the pairs and form a new shorter string from which they will extract the final key. To this end, they run classical post-processing procedures such as error correction and privacy amplification. The amount of privacy amplification needed to securely distil a key depends on the security analysis and the resulting rate equation. In the following, we list the rate equation adopted for each situation analysed in the experiment.

CAL PROTOCOL. This protocol is analysed in the asymptotic scenario for which $P_Z \approx 1$. The corresponding SKR equation is the one given for ‘protocol 3’ in [22] and the procedure we use to calculate it is similar to the one described in [13]. See also [16]. The SKR is the sum of two separate contributions, calculated from each detector D_0 and D_1 independently: $R_{\text{CAL}} = R_{\text{CAL}}^{D_0} + R_{\text{CAL}}^{D_1}$. We write the contribution from D_0 as

$$R_{\text{CAL}}^{D_0} = Q^z [1 - f_{\text{EC}} h(E^z) - h(\bar{e}_1^{\text{ph}})]. \quad (2)$$

The SKR pertaining to D_1 has a similar expression. In Eq. (2), h is the binary entropy function, f_{EC} is the error correction factor and Q^z and E^z are the gain and the bit error rate, respectively, of the protocol, measured in the experiment from the D_0 clicks when the users announce the Z basis. The quantity \bar{e}_1^{ph} is the upper bound to the phase error rate, for which we have [22]

$$\bar{e}_1^{\text{ph}} = \frac{1}{Q^z} \sum_{j=0,1} \left[\sum_{m,n=0}^{N_{\text{cut}}} c_m^{(j)} c_n^{(j)} \sqrt{g_{mn}(\bar{Y}_{mn}^x, Y_{\text{cut}})} \right]^2. \quad (3)$$

In Eq. (3), the coefficient $c_k^{(0)}$ ($c_k^{(1)}$) is defined as $c_k^{(0)} = e^{-\mu/2} \mu^{k/2} / \sqrt{k!}$ when the integer k is even (odd) and 0 otherwise; $g_{mn}(\bar{Y}_{mn}^x, Y_{\text{cut}})$ is a function equal to \bar{Y}_{mn}^x if $m + n < Y_{\text{cut}}$ and equal to 1 otherwise; $Y_{\text{cut}}, N_{\text{cut}}$ are two integers such that $Y_{\text{cut}} < N_{\text{cut}}$. In our experiment we set $Y_{\text{cut}} = 8$ and $N_{\text{cut}} = 12$. The quantities \bar{Y}_{mn}^x are upper bounds for the yields obtained when Alice (Bob) sends m (n) photons. These are estimated using a constrained optimisation linear program [13] similar to the standard decoy state technique [37, 38], with the difference that the yields have to be maximised rather than minimised to provide the worst-case phase error rate. In our implementation, we measured all the intensity combinations uu, uv, uw, vv, vw and ww to improve the decoy-state estimation. In parallel to this numerical estimation, we also implemented the analytical estimation given in [16] to verify the correctness of our results.

SNS PROTOCOL. The SKR for this protocol in the asymptotic scenario ($P_Z \approx 1$) can be written as [24, 29]

$$R_{\text{SNS}} = \underline{Q}_0 + \underline{Q}_1 [1 - h(\bar{e}_1^{\text{ph}})] - f_{\text{EC}} Q^z h(E^z). \quad (4)$$

In Eq. (4), Q^z and E^z are the gain and the bit error rate, respectively, of the protocol, measured in the experiment. The 0-photon gain and 1-photon gain in the Z basis are $\underline{Q}_0 = 2\epsilon(1 - \epsilon)e^{-s}e^{-n}\underline{y}_0$ and $\underline{Q}_1 = 2\epsilon(1 - \epsilon)(se^{-s}e^{-n} + ne^{-n}e^{-s})\underline{y}_1$, respectively. The parameters \underline{y}_1 (\underline{y}_0) and \bar{e}_1^{ph} are, respectively, the lower bound for the single-photon (zero-photon) yield and the upper bound for the single-photon phase error rate. These quantities are drawn from the X basis of the protocol using equations similar to the ones seen in decoy-states QKD [24, 37, 38].

TWCC PROTOCOL. With the addition of two-way classical communication (TWCC), the users can improve the quality of

their data before performing the standard error correction and privacy amplification operations. The SKR in the asymptotic scenario for this protocol is [29]

$$R_{\text{TWCC}} = \frac{1}{N_0} \{ \tilde{n}_1 [1 - h(\tilde{e}_1^{\text{ph}})] - \text{leak}_{\text{EC}} \}, \quad (5)$$

with $\tilde{n}_1 = n_1^2 / (2n_t)$, $\tilde{e}_1^{\text{ph}} = 2\bar{e}_1^{\text{ph}}(1 - \bar{e}_1^{\text{ph}})$, $\text{leak}_{\text{EC}} = f_{\text{EC}}[n_a h(E_a) + n_b h(E_b) + n_c h(E_c)]$. Here, $n_1 = N_0 Q_1$ is the number of untagged bits, i.e. the number of bits generated by Charlie's detections when the users send out single-photon states in the Z basis. $n_t = N_0 Q^z$ is the number of successful detections, an observable of the protocol, with N_0 the total number of prepared states. The term 'leak_{EC}' represents the number of bits to be exchanged during the error correction procedure. The quantities n_a and E_a are the number of bits and the error rate, respectively, in Bob's string associated with an odd parity when paired during the TWCC procedure. Similarly, the quantities n_b and E_b (n_c and E_c) are the number of bits and the error rate, respectively, in Bob's string associated with an even parity and when both bits are 0 (1), when paired during the TWCC procedure. The other quantities are as in Eq. (4).

FINITE-SIZE SNS AND TWCC. The finite size analysis of TWCC [18] is derived directly from the one of SNS [25, 26]. The error correction term of the asymptotic rate equation (5) remains unchanged but the remaining terms are modified to take into account the leakage of information due to finite-size statistical effects. The number of secret bits in the finite-size regime after TWCC has been performed is given by

$$n_{\text{TWCC-FS}} = \hat{n}_1 [1 - h(\hat{e}_1^{\text{ph}})] - \text{leak}_{\text{EC}} - \Delta, \quad (6)$$

with $\Delta = \log_2(2/\epsilon_{\text{EC}}) - 2 \log_2(\sqrt{2}\epsilon_{\text{PA}}\hat{e})$ the finite-size correction term and with ϵ_{EC} , ϵ_{PA} and \hat{e} the failure probabilities for error correction, privacy amplification and the choice of the smoothing parameter, respectively. With the right choice of parameters, our implementation features a security parameter of 2.2×10^{-9} , which is the same as in [18]. The hatted quantities \hat{n}_1 and \hat{e}_1^{ph} correspond to the tilded quantities in Eq. (5), but calculated in the finite-size regime using a composable definition of security and the Chernoff bound. Their detailed expressions can be found in the reference paper [25].

Binary maps generation. From experiments of the SNS TF-QKD protocol described, real keys were extracted. To achieve this, single time-tagged events, acquired in 500 ps windows, were processed individually. Sifting Charlie's announcements, clicks in the Z basis from both detectors were isolated and concatenated. They were then used by Alice and Bob to separately generate their own initial key string. For every photon click recorded in Z basis, Alice (Bob) registers a bit 1 (0) if she (he) had sent a weak-coherent pulse within the time slot and a bit 0 (1) if she (he) had chosen not to send anything. As a result, they obtain matching bits in the cases where only one user has prepared and sent a pulse and opposite bits if both sent. The latter, accompanied by dark counts, contributes to the QBER in the key generation basis. A sample of these initial keys for Alice and Bob are shown in the first two squares of Fig. 4, in the form of binary maps comprised of 128x128 pixels, for the finite-size measurement taken at 522 km. Zeroes and ones are represented by white and black pixels respectively. The white-bias of Alice and black bias of Bob are expected and attributed to the send-clicks that have the highest occurrence probability and

in which Alice will always obtain a 1 while Bob will obtain a 0.

Initial keys were post-processed according to the two-way classical communication method to reduce their initial QBER of 16% and allow successful QKD at such long distances. During this process, Bob's bits are randomly paired up and their parity calculated. The pair positions and resulting parity must be publicly announced so that the procedure can be repeated by Alice who will also announce her results. The initial keys are then further sifted to include only the first bit of pairs whose parity matched in both users. For instance, given the SNS encoding in the key generation basis, pairs encoded as 'sn' by Alice (see Protocols in Methods) in a randomly selected pair will provide a matching parity if paired with bits encoded as 'ns' by Bob whereas will provide unmatched parity if paired with bits encoded as 'ss' by Bob. Although TWCC reduces the length of the secret key, it also significantly reduces the QBER so that the overall signal to noise ratio is increased. The effect of the process on the 522 km data is shown in the first two rectangles at the bottom of Fig. 4. The binary map is reduced in dimension by 70% to represent the equivalent reduction in the entire bit strings. The white, black bias is also visibly reduced. To better depict the QBER reduction the binary maps are bitwise XORed before and after TWCC in the rightmost boxes of Fig. 4. Matching and opposite bits are represented by white and black pixels respectively. In this case, the QBER is reduced by over a factor 4.5, from 16% to 3.5%, thus allowing us to extract a secret key at distances up to 605.2 km.

SUPPLEMENTARY MATERIAL FOR:
 600 KM REPEATER-LIKE QUANTUM COMMUNICATIONS WITH DUAL-BAND STABILISATION

 Mirko Pittaluga^{1,2†*}, Mariella Minder^{1,3†}, Marco Lucamarini^{1,4*}, Mirko Sanzaro¹, Robert I. Woodward¹, Ming-Jun Li⁵, Zhiliang Yuan¹ & Andrew J. Shields¹
¹Toshiba Europe Limited, 208 Cambridge Science Park, Cambridge CB4 0GZ, UK

²School of Electronic and Electrical Engineering, University of Leeds, Leeds LS2 9JT, UK

³Department of Engineering, Cambridge University, 9JJ Thomson Avenue, Cambridge CB3 0FA, UK

⁴Department of Physics and York Centre for Quantum Technologies, University of York, York YO10 5DD, UK

⁵Corning Incorporated, Corning, New York, 14831, USA

[†]These authors contributed equally to this work

*mirko.pittaluga@crl.toshiba.co.uk

*marco.lucamarini@crl.toshiba.co.uk

I. ASYMMETRICAL EXPERIMENTAL SETUP

In Fig. 1 in the main text, the central node (Charlie) owns two lasers and disseminates their optical frequencies to the communicating users (Alice and Bob) in a symmetrical manner. Asymmetrical dissemination is also possible, as shown in Fig. 5. Here, Alice owns two lasers and disseminates their optical frequencies to Bob. The servo fibre becomes a direct link between the users and can bypass Charlie completely. Asymmetry in the optical channels to Charlie can be compensated by inserting a delay fibre to Alice.

An asymmetrical setup benefits from a simpler central node and requiring just one OPLL. We used this asymmetrical configuration consisting of a 51 km servo and 51 km delay fibre for rapid feasibility studies, before adopting the symmetrical setup with 611 km servo fibre in the final experiments.

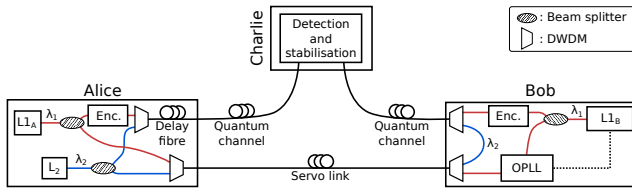


FIG. 5. **Asymmetric TF QKD setup.** Alice disseminates λ_1 and λ_2 wavelengths to Bob. Alice has a delay fibre equalising the servo fibre length. DWDM: dense wavelength division multiplexer or demultiplexer, OPLL: optical phase locked loop, Enc.: encoder, L1_A (L1_B): Laser of Alice (Bob), L₂: laser for bright reference.

II. BLOCK DIAGRAM REPRESENTATION OF THE FEEDBACK SYSTEMS

In Fig. 6 is reported a block diagram representation of the feedback systems used for the phase stabilisation. These systems are discussed in detail in the **Setup** and **Methods** sections of the main text. Figure 6a shows the stabilisation method based on the bright reference at λ_2 . Figure 6b shows the stabilisation mechanism that corrects the residual phase drift on λ_1 .

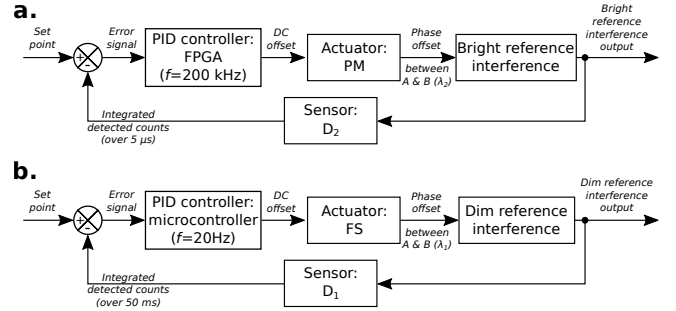


FIG. 6. **Block diagrams of the phase-stabilisation system.** *Top:* Feedback executed on λ_2 . *Bottom:* Feedback executed on λ_1 .

III. SYSTEM CHARACTERISATION

Tab. I reports a detailed characterisation of the experimental setup. This table highlights an asymmetry between the users' insertion losses at Charlie. The asymmetry is related to the two different types of modulators acting on the incoming signals. A phase modulator is lossier than a fibre stretcher (which is almost lossless), and therefore Charlie's system transmission for Bob is lower than for Alice. In the protocol simulations, we used the lowest transmission figure to characterise the losses at the receiver.

In Tab. I we present two different dark counts figures. The first is derived from the SNSPDs (Single Quantum EOS 410 CS cooled at 2.9 K) characterisation, executed with no connected fibre. The second is extracted from the experimental data during protocol execution. We associate the increase in dark counts in the second case mostly to the finite DWDM optical isolation between λ_1 and λ_2 channels, and to the inelastic scattering occurring in the fibres. This figure could be further reduced by using spectral filters with better isolation.

In Tab. II we report the combined losses of the fibre spools used to achieve different quantum channel distances. At all distances, we have assigned the lossier spools to Bob. During the experiment, when there was an asymmetry between the users' photon rate received by Charlie, we compensated for it by increasing the attenuation of Bob's transmitter.

Charlie's system transmission (from Alice)	62.86%
Charlie's system transmission (from Bob)	50.77%
Efficiency SNSPD D_0	73%
Efficiency SNSPD D_1	77%
SNSPD dark counts (calibration)	10 Hz
SNSPD dark counts (experiment)	14 Hz
Clock rate for quantum signal	500 MHz

TABLE I. Experimental parameters of the setup.

Fibre length	Losses (dB)	
	Alice	Bob
76.641 km	13.30	13.25
184.351 km	32.20	31.39
260.866 km	45.39	44.70
277.461 km	48.46	47.73
302.585 km	53.13	52.38

TABLE II. Combined losses of the fibre spools used in the quantum channels.

IV. INTERFERENCE OPTIMISATION

In order to minimise the QBER, it is necessary to optimise the interference between the optical fields prepared by Alice and Bob. Some aspects of this optimisation, such as spectral overlapping (for both λ_1 and λ_2) and time synchronisation (for λ_1), have already been discussed. In this section we will describe the details of the polarisation optimisation routine of the setup, and the optimisation of the λ_2 launch power by the users.

Each user, after executing the encoding over the λ_1 wavelength, aligns their λ_1 and λ_2 signals to the same optical axis through an EPC contained in the Encoder boxes (as discussed in the Methods). They then multiplex these signals together, and provide a pre-compensation for the polarisation rotation

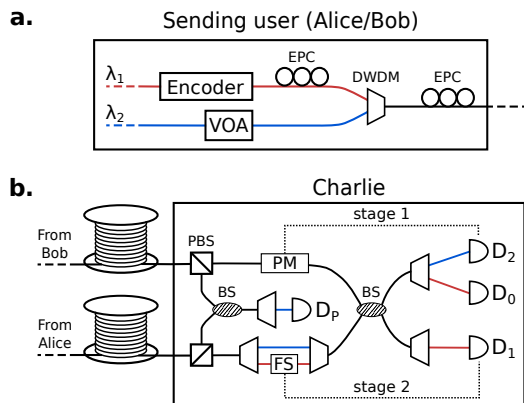


FIG. 7. **Details of polarisation and intensity optimisation.** **a.** equipment for λ_1 and λ_2 polarisation alignment at the users' stations, and for channel polarisation rotation pre-compensation. **b.** equipment for detecting photons in the wrong polarisation at Charlie. BS: beam splitter; D_P , D_0 , D_1 , D_2 : single photon detector; DWDM: dense wavelength division multiplexer/demultiplexer; EPC: electrical polarisation controller; FS: fibre stretcher; PBS: polarisation beam splitter; VOA: variable optical attenuator.

occurring over the quantum channel through a second EPC (see Fig. 7a). For this purpose, Charlie is equipped with two PBSs at the entrance of his station, and of an SNSPD, D_P (see Fig. 7b), whose purpose is detecting the photons arriving with the wrong polarisation. Charlie broadcasts the counts received at D_P over a public channel, and the users take turns in changing their EPCs settings with the aim of minimising the detections at D_P . The users' polarisation optimisation routines are run continuously throughout the protocol execution.

In order to optimise the interference of their λ_2 at Charlie, before running the TF-QKD protocol, each user tunes their λ_2 launch power with the VOA shown in Fig. 7a.

V. NOISE SOURCES IN THE DUAL-BAND STABILISATION TECHNIQUE

The main factors limiting the maximum achievable distance in previous TF-QKD experiments [17, 18] are the difficulty to stabilise phase over increasingly long communication channels, and the noise associated with the time-multiplexed stabilisation strategy. The dual-band stabilisation technique provides a solution to both these problems. It does that by increasing considerably the possible intensity contrast between the stabilisation and the protocol pulses (the contrast is not restricted anymore by the limited range of the intensity modulators, nor by the finite dynamic range of the detectors at Charlie) and by removing double Rayleigh backscattering, the most detrimental source of noise for long-distance time-multiplexed implementations of TF-QKD.

The Rayleigh scattering is a linear process whereby the photons are scattered by the propagation medium. The scattered photons have the same frequency as the original ones, and introduce noise that cannot be filtered out effectively. They are in fact uniformly distributed in time (time filtering is not effective), and have the same wavelength as the quantum pulses (spectral filtering is not effective). In the experiment presented in [18], the authors show that in order to maintain a sufficiently intense stabilisation signal, at ~ 500 km of channel length, the double Rayleigh backscattering starts generating more noise counts than their detectors dark counts. This noise increases with the launch power of the stabilisation signal, which in turn increases with the channel length.

With the dual-band stabilisation technique, the protocol encoded pulses are at a different wavelength than the stabilisation signal, so that the noise due to the double Rayleigh backscattering can be removed (together with the bright stabilisation signal) through spectral filtering. The relevant sources of noise with this approach are the channel cross-talk (from the spectral filters) and Raman scattering.

In our experiment the biggest source of noise is the channel cross-talk. The optical isolation between λ_1 and λ_2 is ~ 52 dB, which introduces ~ 10 Hz of noise in the protocol analysis when we set 8 MHz target count rate at D_2 for the phase stabilisation. This source of noise could be further reduced using spectral filters with better isolation characteristics, or using two filters in series. Different from double Rayleigh backscattering, channel cross-talk depends on the intensity of the received signal at Charlie (which has to be increased at most with the square root of the channel length), rather than on the reference signal's launch power (which has to be increased roughly exponentially with the channel length),

making this noise source much less dependent on the channel length.

The other scattering-related source of noise in our experiment is Raman scattering, which at 600 km contributes by less than 1 Hz to the noise. A figure that could be further reduced by using narrower spectral filters. Similarly to double Rayleigh backscattering, Raman noise increases with the launch power in the channel, but its impact is more than 10 times lower.

VI. ENCODING PARAMETERS

In this experiment we tested different TF-QKD protocols: a phase matching version [22], and the SNS version [24]. The latter, with and without TWCC ([25, 29]). For all the measurements we used a 25040 pulses long pattern. Half of the pulses were used for the protocol encoding (dim quantum). Interleaved to these, phase unmodulated pulses were used as quantum references (dim reference). The pattern encoding was executed by two time-synchronised pattern generators, which controlled the phase and intensity modulators described in the Methods. For every protocol, the pattern properties have been chosen with the aim of maximising the communication distance. With the exception of the point at 505.2 km, the two versions of the TWCC SNS protocol (asymptotic and finite size) used the same pattern over the different tested distances.

The way we encode the patterns is by fair sampling. Using the pattern properties shown in Tab. III and IV, for each protocol we calculate the probabilities of the different users' pulses combinations. At this point, we generate a 12520-elements-long list of pulses pairs reflecting the matching probabilities. This list is then randomly shuffled, resulting in two patterns with a random pulse distribution that respects the matching probabilities expected by the protocol simulations.

Tab. III summarises the photon fluxes and the pattern probabilities used for the CAL TF-QKD protocol. In this protocol the X basis is the one used for coding, while the Z is used for testing (decoy states). Pulses in the X basis can only take two phase values: either $+\pi/2$ or $-\pi/2$. Their intensity is set to be equal to the one of the v decoy pulses. Pulses in the Z basis on the contrary are all phase randomised. Since this protocol has been run only in the asymptotic regime, for the purpose of the key rate estimation, calculations have been carried out by normalising P_X from the original 50% to 99.9%.

Tab. IV summarises the parameters for the different configurations of the SNS TF-QKD protocol we tested. In the SNS protocol, the Z basis is the one used for the key generation

VII. EXPERIMENTAL RESULTS FOR SNS-TYPE PROTOCOLS

In Tab. V, VI, VII, VIII and IX, we report the detailed experimental results for the different SNS-type protocols tested. Data in Tab. V, VI and VII are obtained with the asymmetrical setup (Fig. 5) featuring one OPLL and 51 km servo fibre link. Data in Tab. VIII and IX are collected with the symmetrical setup (Fig. 1 in the main text) consisting of 611 km servo fibre link. Tab. V is reporting the results for the asymptotic SNS protocol (without TWCC). Tab. VI and VIII summarises the results for the TWCC SNS TF-QKD protocol in the asymptotic scenario, while the ones in the finite size regime are reported in Tab. VI and IX.

In all the tables are reported the distances at which the experiments were executed and the number of quantum pulses that

(sending-or-not-sending), while the X basis is used for testing the quantum channel (decoy states). In this protocol, all the encoded pulses (dim quantum) are phase randomised. Also for SNS, in the asymptotic case the key rate estimation was executed by normalising the probability of using the coding basis P_Z from 50% to 99.9%.

Fibre length (km)	CAL asympt.
	368.7
s (ph/pulse)	0.015
u (ph/pulse)	0.1
v (ph/pulse)	0.015
w (ph/pulse)	0.0002
P_Z (code basis)	50.0%
P_X (test basis)	50.0%
P_u	33.3%
P_v	33.3%
P_w	33.3%
Secret key rate	852.7 bps

TABLE III. Secret key rate and parameters used for the implementation of the CAL TF-QKD protocol [22] in the asymptotic scenario. s is the photon flux used for signal pulses, while u, v, w are the photon fluxes used for the decoy states. P_Z is the users' probability of sending a pulse in the code basis. P_X is the users' probability of sending a pulse in the test basis, P_u, P_v, P_w are the probabilities of sending the u, v, w decoy pulses respectively.

Fibre length (km)	SNS asympt.	TWCC SNS asympt.	SNS finite size
	368.7	all except 605	605 all
s (ph/pulse)	0.35	0.35	0.38
u (ph/pulse)	0.35	0.35	0.38
v (ph/pulse)	0.035	0.0105	0.01065
w (ph/pulse)	0.0002	0.0002	0.00023
P_Z (code basis)	50.0%	50.0%	60.0%
P_s	5.8%	13.0%	7.5%
P_X (test basis)	50.0%	50.0%	40.0%
P_u	33.3%	33.3%	20.0%
P_v	33.3%	33.3%	60.0%
P_w	33.3%	33.3%	20.0%

TABLE IV. Parameters of the patterns used for the implementation of the SNS TF-QKD protocol [24] in different experimental scenarios (with or without TWCC [25, 29]), in the asymptotic or finite-size regimes). s is the photon flux used for signal pulses, while u, v, w are the photon fluxes used for the decoy states. P_Z is the users' probability of choosing to encode a pulse in the code basis, P_s is the probability of actually sending a signal when the Z basis is chosen. P_X is the users' probability of encoding a pulse in the test basis, P_u, P_v, P_w are the probabilities of sending the u, v, w decoy pulses respectively.

were sent (N_0). Also reported are the errors in the different bases and for different pulses intensities, and the calculated secret key rate (SKR) obtained at that distance (alongside the relative SKC_0 bound). For all the protocols, the exact number of pulses sent in each pulses pair configuration can be calculated by multiplying the respective configuration probabilities (deducible from Tab. III and IV) by N_0 . The number of pulses detected in these configurations are reported in the tables below, labelled in the format $B_1B_2t_1t_2$, where B_1 and t_1 (B_2 and t_2) are the basis and the type of pulse sent by Alice (Bob). When TWCC is employed, quantities relative to the key post-processing are listed.

Quantum link length (km)	368.702
Servo link length (km)	51.220
N_0	$2.066 \cdot 10^{11}$
Phase mismatch acceptance	22.5°
Z error rate	6.59%
Xuu error rate	3.29%
Xvv error rate	3.87%
Phase error rate	4.15%
SKR SNS (no TWCC) asympt norm (bit/signal)	$1.098 \cdot 10^{-6}$
SKR SNS (no TWCC) asympt norm (bit/s)	$5.492 \cdot 10^2$
Ratio SKR over SKC_0	1.54
SKC_0 (bit/signal)	$7.151 \cdot 10^{-7}$
SKC_0 (bit/s)	$3.576 \cdot 10^2$
Total Detected D_0	4624363
Total Detected D_1	4887891
Detected ZZss	39403
Detected ZZsn	314309
Detected ZZns	304872
Detected ZZnn	4264
Detected ZXsu	217790
Detected ZXsv	121824
Detected ZXsw	112334
Detected ZXnu	1729304
Detected ZXnv	173107
Detected ZXnw	1634
Detected XZus	217780
Detected XZun	1786996
Detected XZvs	117638
Detected XZvn	155240
Detected XZws	113964
Detected XZwn	1486
Detected XXuu	1240351
Detected XXuv	685682
Detected XXuw	643480
Detected XXvu	668424
Detected XXvv	115296
Detected XXvw	55695
Detected XXwu	628786
Detected XXwv	62043
Detected XXww	552
Detected XXuu matching (D_0)	74844
Detected XXuu matching (D_1)	79037
Correct XXuu matching (D_0)	72352
Correct XXuu matching (D_1)	76474
Detected ZZ errors	43667
Detected ZZ correct	619181

TABLE V. Asymptotic SNS: experimental results for a quantum link length of 368.7 km and a servo link length of 51 km.

Quantum link length (km)	153.282	368.702	521.982	555.172	605.170
Servo link length (km)	51.220	51.220	51.220	51.220	51.220
N_0	$5.296 \cdot 10^{10}$	$1.527 \cdot 10^{11}$	$5.208 \cdot 10^{11}$	$2.554 \cdot 10^{11}$	$1.002 \cdot 10^{12}$
Phase mismatch acceptance	22.5°	22.5°	22.5°	22.5°	22.5°
Z error rate (before)	13.1%	13.1%	14.%	14.6%	16.4%
Odd pairs in raw keys	$3.522 \cdot 10^6$	$2.277 \cdot 10^5$	$3.968 \cdot 10^4$	$9.565 \cdot 10^3$	$1.369 \cdot 10^4$
Even pairs 00 in raw keys	$1.938 \cdot 10^6$	$1.228 \cdot 10^5$	$2.162 \cdot 10^4$	$5.174 \cdot 10^3$	$7.411 \cdot 10^3$
Even pairs 11 in raw keys	$1.74 \cdot 10^6$	$1.15 \cdot 10^5$	$1.963 \cdot 10^4$	$4.725 \cdot 10^3$	$6.575 \cdot 10^3$
Error pairs in raw keys	$1.591 \cdot 10^5$	$1.039 \cdot 10^4$	$2.096 \cdot 10^3$	$5.532 \cdot 10^2$	$1.029 \cdot 10^3$
Z error rate (after)	2.21%	2.23%	2.59%	2.84%	3.72%
Xuu error rate	2.8%	3.21%	3.86%	3.68%	3.5%
Xvv error rate	5.53%	6.32%	4.78%	8.33%	13.6%
Phase error rate	5.68%	6.4%	3.71%	6.08%	2.31%
n_1 (before TWCC)	$1.159 \cdot 10^7$	$7.49 \cdot 10^5$	$1.254 \cdot 10^5$	$3.284 \cdot 10^4$	$3.733 \cdot 10^4$
n_1 (after TWCC)	$3.605 \cdot 10^6$	$2.326 \cdot 10^5$	$3.685 \cdot 10^4$	$1.04 \cdot 10^4$	$9.136 \cdot 10^3$
e_1^{ph} (before TWCC)	5.68%	6.4%	3.71%	6.08%	2.31%
e_1^{ph} (after TWCC - asympt)	10.7%	12.%	7.15%	11.4%	4.52%
SKR TWCC asympt norm (bit/signal)	$7.441 \cdot 10^{-5}$	$1.412 \cdot 10^{-6}$	$8.557 \cdot 10^{-8}$	$2.838 \cdot 10^{-8}$	$1.937 \cdot 10^{-9}$
SKR TWCC asympt norm (bit/s)	$3.721 \cdot 10^4$	$7.059 \cdot 10^2$	$4.278 \cdot 10^1$	$1.419 \cdot 10^1$	$9.685 \cdot 10^{-1}$
Ratio SKR over SKC ₀	0.0215	1.97	50.	61.3	29.7
SKC ₀ (bit/signal)	$3.456 \cdot 10^{-3}$	$7.151 \cdot 10^{-7}$	$1.711 \cdot 10^{-9}$	$4.632 \cdot 10^{-10}$	$6.511 \cdot 10^{-11}$
SKC ₀ (bit/s)	$1.728 \cdot 10^6$	$3.576 \cdot 10^2$	$8.556 \cdot 10^{-1}$	$2.316 \cdot 10^{-1}$	$3.256 \cdot 10^{-2}$
Total Detected D_0	66051719	4241991	745698	181085	263766
Total Detected D_1	69221704	4524664	795437	193156	278746
Detected ZZss	2423210	156953	27876	6727	9620
Detected ZZsn	8146041	521082	91891	22168	32219
Detected ZZns	8052039	526583	91497	22122	31538
Detected ZZnn	11389	1380	2024	848	2907
Detected ZXsu	6196623	403188	70879	17076	24785
Detected ZXsv	3217021	205870	36367	8629	12876
Detected ZXsw	3107274	198690	35299	8610	12320
Detected ZXnu	20581340	1349062	235655	57121	81690
Detected ZXnv	604012	37884	7635	1915	3125
Detected ZXnw	4212	518	747	289	1085
Detected XZus	6202770	403207	70119	17168	24722
Detected XZun	20928197	1340008	236339	57217	82636
Detected XZvs	3181382	208453	36111	8811	12607
Detected XZvn	628269	41662	7104	1879	3037
Detected XZws	3078177	202140	35286	8426	12396
Detected XZwn	4250	534	765	281	1102
Detected XXuu	15759404	1022280	179333	43000	61766
Detected XXuv	8202418	526279	92761	22151	32573
Detected XXuw	7977865	511560	89706	21900	31585
Detected XXvu	8127297	531576	92456	22577	31672
Detected XXvv	480868	30579	5527	1427	1904
Detected XXvw	247965	16325	2809	799	1182
Detected XXwu	7874039	516027	89699	22269	31572
Detected XXwv	235716	14614	2968	718	1170
Detected XXww	1645	201	282	113	423
Detected XXuu matching (D_0)	930327	59658	10558	2581	3712
Detected XXuu matching (D_1)	990284	64565	11389	2746	3939
Correct XXuu matching (D_0)	905683	57844	10179	2478	3594
Correct XXuu matching (D_1)	961135	62388	10921	2653	3789
Detected ZZ errors	2434599	158333	29900	7575	12527
Detected ZZ correct	16198080	1047665	183388	44290	63757

TABLE VI. Asymptotic TWCC SNS: experimental results obtained with a 51 km servo link for various quantum link fibre lengths.

Quantum link length (km)	153.282	368.702	521.982	555.172
Servo link length (km)	51.220	51.220	51.220	51.220
N_0	$6.000 \cdot 10^{11}$	$2.435 \cdot 10^{12}$	$3.070 \cdot 10^{12}$	$3.536 \cdot 10^{12}$
Phase mismatch acceptance	22.5°	22.5°	22.5°	22.5°
Z error rate (before)	7.67%	7.69%	9.01%	9.77%
Odd pairs in raw keys	$4.164 \cdot 10^7$	$3.564 \cdot 10^6$	$2.333 \cdot 10^5$	$1.336 \cdot 10^5$
Even pairs 00 in raw keys	$2.135 \cdot 10^7$	$1.838 \cdot 10^6$	$1.198 \cdot 10^5$	$6.922 \cdot 10^4$
Even pairs 11 in raw keys	$2.077 \cdot 10^7$	$1.768 \cdot 10^6$	$1.152 \cdot 10^5$	$6.501 \cdot 10^4$
Error pairs in raw keys	$5.738 \cdot 10^5$	$4.938 \cdot 10^4$	$4.542 \cdot 10^3$	$3.103 \cdot 10^3$
Z error rate (after)	0.685%	0.689%	0.97%	1.16%
Xuu error rate	2.69%	2.88%	2.87%	3.47%
Xvv error rate	3.56%	3.81%	5.31%	5.09%
Phase error rate	4.16%	4.47%	6.04%	5.59%
n_1 (before TWCC)	$1.185 \cdot 10^8$	$1.003 \cdot 10^7$	$6.4 \cdot 10^5$	$3.652 \cdot 10^5$
n_1 (after TWCC)	$3.596 \cdot 10^7$	$3.013 \cdot 10^6$	$1.828 \cdot 10^5$	$1.026 \cdot 10^5$
e_1^{ph} (before TWCC)	4.23%	4.71%	7.48%	7.65%
e_1^{ph} (after TWCC)	8.09%	8.98%	13.8%	14.1%
Number of secure bits generated (bits)	$1.707 \cdot 10^7$	$1.329 \cdot 10^6$	$4.046 \cdot 10^4$	$1.745 \cdot 10^4$
SKR (bit/signal)	$2.846 \cdot 10^{-5}$	$5.459 \cdot 10^{-7}$	$1.318 \cdot 10^{-8}$	$4.937 \cdot 10^{-9}$
SKR (bit/s)	$1.423 \cdot 10^4$	$2.729 \cdot 10^2$	6.59	2.468
Ratio SKR over SKC ₀	0.00823	0.763	7.7	10.7
SKC ₀ (bit/signal)	$3.456 \cdot 10^{-3}$	$7.151 \cdot 10^{-7}$	$1.711 \cdot 10^{-9}$	$4.632 \cdot 10^{-10}$
SKC ₀ (bit/s)	$1.728 \cdot 10^6$	$3.576 \cdot 10^2$	$8.556 \cdot 10^{-1}$	$2.316 \cdot 10^{-1}$
Total Detected D_0	601407532	50532067	3317070	1945930
Total Detected D_1	623261177	54266217	3616047	2071809
Detected ZZss	14322977	1229675	80689	46061
Detected ZZsn	90153430	7739935	511622	296484
Detected ZZns	90035335	7685653	507468	290238
Detected ZZnn	642059	54944	20176	17462
Detected ZXsu	25714805	2199489	144929	82891
Detected ZXsv	46330397	3956642	262219	150458
Detected ZXsw	12870272	1107377	72977	42765
Detected ZXnu	159718589	13637478	898693	517464
Detected ZXnv	90956994	7710475	507227	297300
Detected ZXnw	93804	7989	2973	2550
Detected XZus	25704406	2209257	146032	85067
Detected XZun	159575781	13695784	906734	526484
Detected XZvs	46091214	3944702	259209	149050
Detected XZvn	89990485	7718247	507676	294097
Detected XZws	12982067	1109205	73179	42204
Detected XZwn	92445	7776	2977	2516
Detected XXuu	44724005	3838050	252841	145782
Detected XXuv	82278922	7047247	466076	270776
Detected XXuw	22992576	1978960	131444	75985
Detected XXvu	82116355	7042214	463506	268561
Detected XXvv	78177798	6684280	437657	252988
Detected XXvw	13010771	1116305	73487	42281
Detected XXwu	22952199	1964545	129678	75082
Detected XXwv	13127709	1110997	73238	42795
Detected XXww	13314	1058	410	398
Detected XXuu matching (D_0)	2822546	239368	15656	9148
Detected XXuu matching (D_1)	2880087	250202	16753	9609
Correct XXuu matching (D_0)	2743311	232285	15215	8846
Correct XXuu matching (D_1)	2805790	243186	16263	9260
Detected ZZ errors	14965036	1284619	100865	63523
Detected ZZ correct	180188765	15425588	1019090	586722

TABLE VII. Finite-size TWCC SNS: experimental results obtained with a servo link length of 51 km at various quantum link fibre lengths.

Quantum link length (km)	555.172	605.170
Servo link length (km)	611.448	611.448
N_0	$8.038 \cdot 10^{11}$	$1.353 \cdot 10^{12}$
Phase mismatch acceptance	22.5°	22.5°
Z error rate (before)	14.1%	16.3%
Odd pairs in raw keys	$2.622 \cdot 10^4$	$1.631 \cdot 10^4$
Even pairs 00 in raw keys	$1.445 \cdot 10^4$	$8.530 \cdot 10^3$
Even pairs 11 in raw keys	$1.272 \cdot 10^4$	$8.134 \cdot 10^3$
Error pairs in raw keys	$1.412 \cdot 10^3$	$1.205 \cdot 10^3$
Z error rate (after)	2.64%	3.65%
Xuu error rate	4.99%	5.41%
Xvv error rate	9.68%	13.0%
Phase error rate	5.12%	5.94%
n_1 (before TWCC)	$8.615 \cdot 10^4$	$5.346 \cdot 10^4$
n_1 (after TWCC)	$2.631 \cdot 10^4$	$1.5756 \cdot 10^4$
e_1^{ph} (before TWCC)	5.12%	5.94%
e_1^{ph} (after TWCC - asympt)	9.71%	11.2%
SKR TWCC asympt norm (bit/signal)	$2.936 \cdot 10^{-8}$	$1.555 \cdot 10^{-9}$
SKR TWCC asympt norm (bit/s)	$1.468 \cdot 10^1$	$7.778 \cdot 10^{-1}$
Ratio SKR over SKC ₀	63.4	24.0
SKC ₀ (bit/signal)	$4.632 \cdot 10^{-10}$	$6.468 \cdot 10^{-11}$
SKC ₀ (bit/s)	$2.316 \cdot 10^{-1}$	$3.234 \cdot 10^{-2}$
Total Detected D_0	494716	312237
Total Detected D_1	523903	329627
Detected ZZss	18133	11390
Detected ZZsn	61210	37648
Detected ZZns	59884	38261
Detected ZZnn	1822	3392
Detected ZXsu	46849	28773
Detected ZXsv	24278	14942
Detected ZXsw	23458	14489
Detected ZXnu	153672	96970
Detected ZXnv	4919	4045
Detected ZXnw	685	1319
Detected XZus	46598	28882
Detected XZun	157244	96571
Detected XZvs	23398	14948
Detected XZvn	4967	4004
Detected XZws	22942	14598
Detected XZwn	686	1371
Detected XXuu	118175	73243
Detected XXuv	62210	38161
Detected XXuw	60417	36867
Detected XXvu	60505	38517
Detected XXvv	3671	2582
Detected XXvw	2015	1588
Detected XXwu	58686	37257
Detected XXwv	1940	1548
Detected XXww	255	498
Detected XXuu matching (D_0)	6963	4178
Detected XXuu matching (D_1)	7452	4358
Correct XXuu matching (D_0)	6624	3974
Correct XXuu matching (D_1)	7071	4100
Detected ZZ errors	19955	14782
Detected ZZ correct	121094	75909

TABLE VIII. Asymptotic TWCC SNS with 611 km servo link: experimental results obtained at various quantum link fibre lengths.

Quantum link length (km)	555.172
Servo link length (km)	611.448
N_0	$3.121 \cdot 10^{12}$
Phase mismatch acceptance	22.5°
Z error rate (before)	9.98%
Odd pairs in raw keys	$9.163 \cdot 10^4$
Even pairs 00 in raw keys	$4.608 \cdot 10^4$
Even pairs 11 in raw keys	$4.594 \cdot 10^4$
Error pairs in raw keys	$2.234 \cdot 10^3$
Z error rate (after)	1.22%
Xuu error rate	5.12%
Xvv error rate	5.49%
Phase error rate	5.73%
n_1 (before TWCC)	$2.597 \cdot 10^5$
n_1 (after TWCC)	$7.530 \cdot 10^4$
e_1^{ph} (before TWCC)	8.32%
e_1^{ph} (after TWCC)	15.2%
Number of secure bits generated (bits)	$1.109 \cdot 10^4$
SKR (bit/signal)	$3.555 \cdot 10^{-9}$
SKR (bit/s)	1.777
Ratio SKR over SKC ₀	7.675
SKC ₀ (bit/signal)	$4.632 \cdot 10^{-10}$
SKC ₀ (bit/s)	$2.316 \cdot 10^{-1}$
Total Detected D_0	1330784
Total Detected D_1	1429497
Detected ZZss	31819
Detected ZZsn	200662
Detected ZZns	202447
Detected ZZnn	12911
Detected ZXsu	57243
Detected ZXsv	103341
Detected ZXsw	28818
Detected ZXnu	357386
Detected ZXnv	209380
Detected ZXnw	1823
Detected XZus	57723
Detected XZun	354724
Detected XZvs	102785
Detected XZvn	203294
Detected XZws	29110
Detected XZwn	1825
Detected XXuu	99664
Detected XXuv	183501
Detected XXuw	51213
Detected XXvu	183158
Detected XXvv	175638
Detected XXvw	29287
Detected XXwu	51513
Detected XXwv	30769
Detected XXww	247
Detected XXuu matching (D_0)	5842
Detected XXuu matching (D_1)	6417
Correct XXuu matching (D_0)	5529
Correct XXuu matching (D_1)	6102
Detected ZZ errors	44730
Detected ZZ correct	403109

TABLE IX. Finite-size TWCC SNS with and 555.2 km quantum link fibre and 611 km servo fibre.